Computer-generated holographic optical tweezer arrays

Eric R. Dufresne
Department of Physics, James Franck Institute, and Institute for Biophysical Dynamics, The University of Chicago, Chicago, Illinois 60637

Gabriel C. Spalding, Matthew T. Dearing, and Steven A. Sheets
Department of Physics, Illinois Wesleyan University, Bloomington, Illinois 61702

David G. Grier[a)]
Department of Physics, James Franck Institute, and Institute for Biophysical Dynamics, The University of Chicago, Chicago, Illinois 60637

(Received 25 August 2000; accepted for publication 4 December 2000)

Holographic techniques significantly extend the capabilities of laser tweezing, making possible extended trapping patterns for manipulating large numbers of particles and volumes of soft matter. We describe practical methods for creating arbitrary configurations of optical tweezers using computer-generated diffractive optical elements. While the discussion focuses on ways to create planar arrays of identical tweezers, the approach can be generalized to three-dimensional arrangements of heterogeneous tweezers and extended trapping patterns. © *2001 American Institute of Physics.* [DOI: 10.1063/1.1344176]

I. INTRODUCTION

Since their invention in 1986,[1] optical tweezers have become increasingly valuable tools for research in the biological[2] and physical[3] sciences. Using a focused beam of light to trap and move matter, optical tweezers offer convenient, noninvasive access to processes at the mesoscopic scale. Most applications, however, have involved manipulating small numbers of particles or small volumes of soft materials because existing optical tweezer implementations can create just a few tweezers at once. Were they readily available, large arrays of optical tweezers could be used to organize microscopic particles into complex structures, to sort them intelligently, to study collective behavior in many-body systems, and to manipulate materials too delicate to trap with a single tweezer. We recently described[4] a method to create arrays of optical tweezers using computer-generated holographic beam splitters. This article further explains how to design and fabricate the necessary holograms and how to integrate them into *holographic optical tweezer arrays* capable of trapping hundreds of particles simultaneously.

II. OPTICS OF OPTICAL TWEEZERS

An optical tweezer traps particles with forces generated by optical intensity gradients. Dielectric particles polarized by the light's electric field are drawn up the gradients to the brightest point. Reflecting, absorbing and low-dielectric particles, by contrast, are driven by radiation pressure to the darkest point. Optically generated forces strong enough to form a three-dimensional trap can be obtained by bringing a laser beam with an appropriately shaped wave front to a tight focus with a high numerical aperture lens. Microscope objective lenses offer an ideal combination of minimal aberration and large numerical aperture and often serve as the focusing element in practical implementations of optical tweezers[1] and variants such as the optical vortex.[5,6]

The challenge in constructing an optical tweezer is to direct a laser beam into the objective lens' back aperture so that the beam fills the aperture and so that its axis coincides with the optical axis in the aperture's plane, at the point labeled B in Fig. 1. If the beam follows the optical axis, then it comes to a focus and forms a trap in the center of the lens' focal plane. If, on the other hand, it enters the back aperture at an angle, the resulting trap is offset from the center of the focal plane, as indicated schematically in Fig. 1.

Directing the beam into the objective with a dichroic mirror allows other wavelengths to pass through unimpeded and can be useful for imaging the trapped particles, as in Fig. 1. The problem remains, however, of aiming the beam.

The telescope formed by lenses L1 and L2 in Fig. 1 addresses this problem by creating a conjugate point, B*, to the back aperture's center, B, at a convenient location. A beam of light passing through B*also passes through B and forms an optical trap. In our implementation, L1 and L2 are high quality plano-convex lenses with 250 mm focal lengths. Such long focal lengths help to minimize aberrations, particularly longitudinal spherical aberration, which would be detrimental to trapping.[7–9] More compact optical trains would require additional attention to minimizing wave front distortions. References 10 and 11 offer more detailed discussions of this aspect of the optical design.

Multiple beams passing through B*all pass through B and thus all form optical tweezers. A diffractive optical element (DOE) at B*, as shown in Fig. 1, can split a single collimated laser beam into any desired distribution of beams, each emanating from B* at a different angle, and thus each forming a separate trap.[4] Figure 1 shows the computer-generated pattern for a binary phase hologram together with

[a)]Electronic mail: grier@fafnir.uchicago.edu

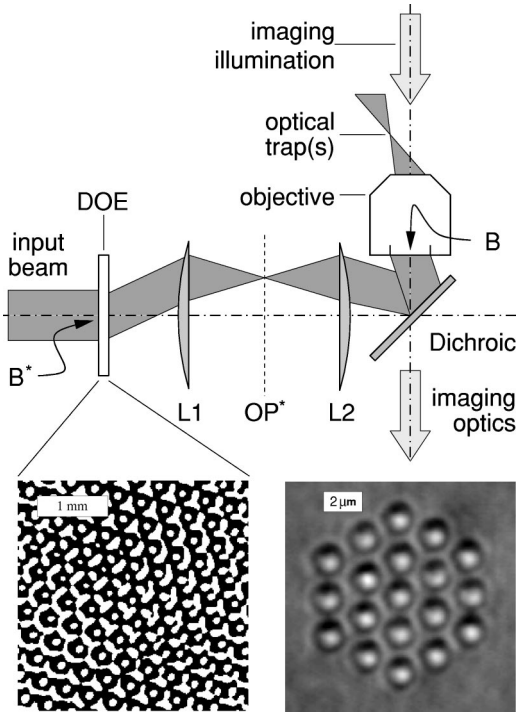

FIG. 1. Schematic representation of a typical holographic optical tweezer array. A collimated laser beam incident from the left is shaped by a diffractive optical element (DOE), transferred to an objective lens' back aperture (B) by lenses L1 and L2 and focused into a trapping array. OP* denotes the plane conjugate to the trapping plane. The point B*is conjugate to B. The phase pattern on the lower left (black regions shift the phase by π radians) produced the traps shown in the lower right filled with 1-μm-diam silica spheres suspended in water.

a photomicrograph of colloidal particles trapped in the resulting array of optical tweezers. The remainder of this article addresses the theory and practice of creating holograms such as the example in Fig. 1 suitable for projecting arbitrary arrangements of optical tweezers.

III. HOLOGRAPHIC TWEEZER ARRAYS

A. Fourier optics

A planar array of optical tweezers can be described by the intensity distribution, $I^f(\boldsymbol{\rho})$, of laser light in the focal plane of a microscope's objective lens. This pattern is determined by the electric field of light incident at its input plane, as depicted in Fig. 2. Suppose that the input plane is illuminated by monochromatic light of wavelength λ. Its wave front at the input plane, $E^{\text{in}}(\mathbf{r})$, contains both phase and amplitude information

$$E^{\text{in}}(\mathbf{r}) = A^{\text{in}}(\mathbf{r}) \exp[i\Phi^{\text{in}}(\mathbf{r})], \tag{1}$$

where the amplitude, $A^{\text{in}}(\mathbf{r})$, and phase, $\Phi^{\text{in}}(\mathbf{r})$, are real-valued functions. The electric field in the focal plane has a similar form,

$$E^f(\boldsymbol{\rho}) = A^f(\boldsymbol{\rho}) \exp[i\Phi^f(\boldsymbol{\rho})], \tag{2}$$

so that $I^f(\boldsymbol{\rho}) = |E^f(\boldsymbol{\rho})|^2 = |A^f(\boldsymbol{\rho})|^2$. These fields are related by the Fourier transform pair

$$E^f(\boldsymbol{\rho}) = \frac{k}{2\pi f} e^{i\theta(\boldsymbol{\rho})} \int d^2r\, E^{\text{in}}(\mathbf{r})\, e^{-ik\mathbf{r}\cdot\boldsymbol{\rho}/f} \tag{3}$$

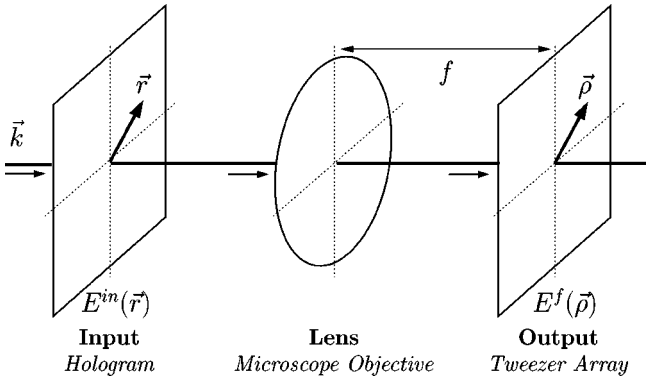

FIG. 2. Schematic representation of the optical train highlighting the relationship between the beam geometry in the input and focal planes. Monochromatic light, with wave vector **k**, is incident on the input plane. A lens of focal length f projects the Fourier transform of the incident light's wave front onto the focal plane.

$$\equiv \mathcal{F}\{E^{\text{in}}(\mathbf{r})\} \quad \text{and} \tag{4}$$

$$E^{\text{in}}(\mathbf{r}) = \frac{k}{2\pi f} \int d^2\rho\, e^{-i\theta(\boldsymbol{\rho})} E^f(\boldsymbol{\rho})\, e^{ik\mathbf{r}\cdot\boldsymbol{\rho}/f} \tag{5}$$

$$\equiv \mathcal{F}^{-1}\{E^f(\boldsymbol{\rho})\}, \tag{6}$$

where f is the focal length of the lens and $k = 2\pi/\lambda$ is the wave number of the incident light. The additional phase profile, $\theta(\boldsymbol{\rho})$, due to the lens' geometry does not contribute to $I^f(\boldsymbol{\rho})$ and may be ignored without loss of generality.[12]

B. Phase-only holograms

Obtaining a desired wave front in the focal plane requires introducing the appropriate wave front in the input plane. Most lasers, however, provide only a fixed wave front,

$$E_0(\mathbf{r}) = A_0(\mathbf{r}) \exp[i\Phi_0(\mathbf{r})]. \tag{7}$$

Shaping $E_0(\mathbf{r})$ into $E^{\text{in}}(\mathbf{r})$ involves modifying both the amplitude and phase at the input plane. Changing the amplitude with a passive optical element necessarily diverts power from the beam and diminishes trapping efficiency. Fortunately, optical trapping relies on the beam's intensity and not on its phase. We can exploit this redundancy by setting $A^{\text{in}}(\mathbf{r}) = A_0(\mathbf{r})$ and modulating only the phase of the input beam to obtain the desired trapping configuration.

Several techniques are available for achieving the necessary phase modulation, and some of the associated practical considerations are discussed in Sec. VI. For the purposes of the present discussion, we will refer to the phase modulating element as a hologram or a diffractive optical element and treat it as if it acts in transmission, as shown in Fig. 1.

After passing through a phase modulating hologram, the electric field in the input plane has a modified wave front

$$E^{\text{in}}(\mathbf{r}) = E_0(\mathbf{r}) \exp[i\Phi^{\text{in}}(\mathbf{r})], \tag{8}$$

where $\Phi^{\text{in}}(\mathbf{r})$ is the imposed phase profile. Calculating the phase hologram, $\Phi^{\text{in}}(\mathbf{r})$, needed to project a desired pattern of traps is not particularly straightforward, as a simple example demonstrates.

In a typical application of holographic optical tweezer arrays, the undiffracted beam, $E_0(\mathbf{r})$, projects a single optical

tweezer into the center of the focal plane with output wave front $E_0^f(\boldsymbol{\rho})$, and the goal is to create displaced copies of this tweezer in the focal plane. One possible wave front describing an array of N optical tweezers at positions $\boldsymbol{\rho}_i$ in the focal plane is a superposition of single (nonoverlapping) tweezers

$$E^f(\boldsymbol{\rho}) = \sum_{i=1}^{N} \alpha_i E_0^f(\boldsymbol{\rho} - \boldsymbol{\rho}_i), \tag{9}$$

where the normalization $\Sigma_{i=1}^{N} |\alpha_i|^2 = 1$ conserves energy. $E^f(\boldsymbol{\rho})$ may be written as a convolution

$$E^f(\boldsymbol{\rho}) = \int d^2\rho' \, E_0^f(\boldsymbol{\rho}') \, T(\boldsymbol{\rho} - \boldsymbol{\rho}') \tag{10}$$

$$\equiv E_0^f \circ T(\boldsymbol{\rho}) \tag{11}$$

of $E_0^f(\boldsymbol{\rho})$ with a lattice function

$$T(\boldsymbol{\rho}) = \sum_{i=1}^{N} \alpha_i \, \delta^{(2)}(\boldsymbol{\rho} - \boldsymbol{\rho}_i). \tag{12}$$

Equations (6) and (8) relate $E^f(\boldsymbol{\rho})$ to the associated input wave front

$$E_0^{\text{in}}(\mathbf{r}) \exp[i\Phi^{\text{in}}(\mathbf{r})] = \mathcal{F}^{-1}\{E_0^f \circ T(\boldsymbol{\rho})\} \tag{13}$$

$$= \frac{2\pi f}{k} \mathcal{F}^{-1}\{E_0^f(\boldsymbol{\rho})\} \, \mathcal{F}^{-1}\{T(\boldsymbol{\rho})\} \tag{14}$$

by the Fourier convolution theorem. The phase modulation needed to achieve the array of optical tweezers then follows from Eq. (8):

$$\exp[i\Phi^{\text{in}}(\mathbf{r})] = \frac{2\pi f}{k} \mathcal{F}^{-1}\{T(\boldsymbol{\rho})\}, \tag{15}$$

independent of the form of the single tweezer.

The phases of the complex weights, α_i, must be selected so that $\Phi^{\text{in}}(\mathbf{r})$ is a real-valued function. Unfortunately, the resulting system of equations has no analytic solution. Still greater difficulties are encountered in designing more general systems of optical traps, including tweezers which trap out of the focal plane or mixed arrays of conventional and vortex tweezers. Rather than deriving solutions for particular tweezer configurations, we have developed more general numerical methods which we apply in the following sections to creating planar arrays optical tweezers.

IV. ADAPTIVE-ADDITIVE ALGORITHM

Our approach is based on the adaptive-additive (AA) algorithm of Soifer, Kotlyar, and Doskolovich,[13] an iterative numerical technique which explores the space of degenerate phase profiles, $\Phi^f(\boldsymbol{\rho})$, to find a phase modulation of the incident laser beam encoding any desired intensity profile in the focal plane. To facilitate calculation and fabrication, both the input and output planes are discretized into $M \times M$ square arrays of pixels. Optimal spatial resolution requires pixels in the focal plane to be one half wavelength on a side, $\delta^f = \lambda/2$. The number, M, of pixels on a side then depends on the desired dimensions of the trapping array. Lengths in the input and focal planes are related by Eqs. (4) and (6), so that

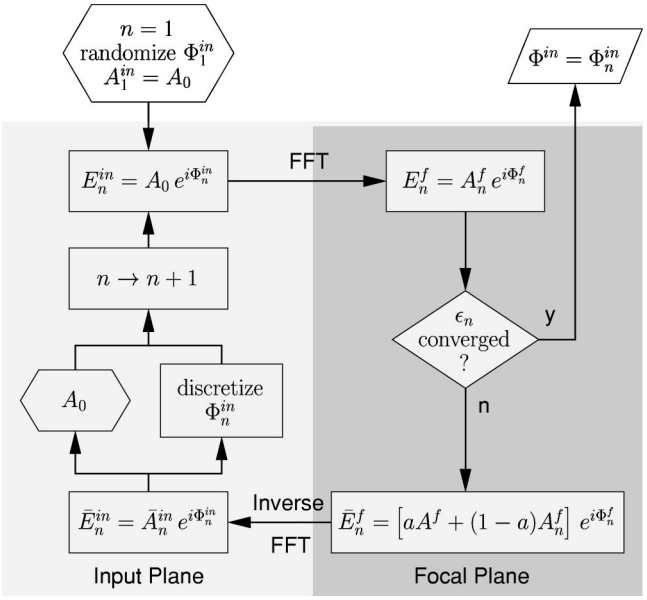

FIG. 3. Flow chart for the adaptive-additive algorithm. The phase modulation, $\Phi_n^{\text{in}}(\mathbf{r})$, can be quantized into discrete steps with every iteration, as shown, or after the algorithm has converged.

the corresponding pixel size in the input plane is $\delta^{\text{in}} = \lambda f/(M\delta^f) = 2f/M$. If δ^{in} is inconveniently small, then L1 and L2 can be chosen so that a more amenable pixel size in the input plane corresponds to δ^f in the focal plane.

The AA algorithm, depicted in Fig. 3, starts with an arbitrary initial guess for $\Phi_1^{\text{in}}(\mathbf{r})$ and an initial input wave front $E_1^{\text{in}}(\mathbf{r}) = E_0(\mathbf{r}) \exp[i\Phi_1^{\text{in}}(\mathbf{r})]$. The Fourier transform of this wave front is the starting estimate for the output electric field: $E_1^f(\boldsymbol{\rho}) = \mathcal{F}\{E_1^{\text{in}}(\mathbf{r})\} = A_1^f(\boldsymbol{\rho}) \exp[i\Phi_1^f(\boldsymbol{\rho})]$. The corresponding intensity in the output plane, $I_1^f(\boldsymbol{\rho}) = |A_1^f(\boldsymbol{\rho})|^2$ is unlikely to be a good rendition of the desired intensity pattern, $I^f(\boldsymbol{\rho}) = |A^f(\boldsymbol{\rho})|^2$. The error

$$\epsilon_1 \equiv \frac{1}{M^2} \sum_{i=1}^{M^2} [I^f(\boldsymbol{\rho}_i) - I_1^f(\boldsymbol{\rho}_i)]^2, \tag{16}$$

is reduced by mixing a proportion, a, of the desired amplitude into the field in the focal plane

$$\overline{E_1^f}(\boldsymbol{\rho}) = [aA^f(\boldsymbol{\rho}) + (1-a)A_1^f(\boldsymbol{\rho})] \exp[i\Phi_1^f(\boldsymbol{\rho})]. \tag{17}$$

Inverse transforming $\overline{E_1^f}(\boldsymbol{\rho})$ yields the corresponding field in the input plane, $\overline{E_1^{\text{in}}}(\mathbf{r}) = \overline{A_1^{\text{in}}}(\mathbf{r}) \exp[i\Phi_2^{\text{in}}(\mathbf{r})]$. At this point, the amplitude in the input plane no longer matches the actual laser profile, so we replace $\overline{A_1^{\text{in}}}(\mathbf{r})$ with $A_0(\mathbf{r})$. The result is an improved estimate for the input field: $E_2^{\text{in}}(\mathbf{r}) = E_0(\mathbf{r}) \exp[i\Phi_2^{\text{in}}(\mathbf{r})]$. This completes one iteration of the AA algorithm. Subsequent iterations lead to monotonically improving estimates, $\Phi_n^{\text{in}}(\mathbf{r})$, for the desired phase modulation.[13] The cycle is repeated until the error, ϵ_n, in the nth iteration converges to within an acceptable tolerance: $(\epsilon_n - \epsilon_{n-1})/\epsilon_n < \chi$.

The phase and amplitude fields are computed as arrays of double-precision numbers, and their Fourier transforms calculated with fast Fourier transform (FFT) routines. Starting from random input phases, $\Phi_1^{\text{in}}(\mathbf{r}_i)$, uniformly distributed

in the range 0 to 2π, the AA algorithm typically requires eight iterations to converge within $\chi = 10^{-6}$ of an acceptably accurate local minimum of ϵ_n using an intermediate value for the mixing parameter, $a = 0.5$.

V. PRACTICAL CONSIDERATIONS

The AA algorithm generates phase profiles, $\Phi^{\text{in}}(\mathbf{r})$, that vary continuously between 0 and 2π. Actually creating a phase element with continuously varying phase delay is difficult; usually only a small number of discrete levels are available. Discretizing the output of the adaptive-additive algorithm necessarily introduces errors. These can be minimized by integrating the discretization step into the AA algorithm itself, as shown in Fig. 3, although this can lead to problems with convergence.

A. Binarization

The most straightforward phase modulators offer just two levels of phase delay, and are known as binary holograms. Beyond quantization errors and their attendant loss of efficiency, binarization also imposes inversion symmetry on the output wave front, $E^f(\boldsymbol{\rho}) = E^f(-\boldsymbol{\rho})$, and so limits what patterns can be generated. This might not seem a problem for inversion-symmetric patterns, but interference between two sides of the pattern can lead to unsatisfactory results, as shown in Figs. 4(a) and 4(b). If, however, we anticipate the reflection and calculate a phase mask encoding only half of the array, we achieve much better results, as shown in Figs. 4(c) and 4(d). In practice, we repeat this calculation about 20 times and choose the binary hologram with the best performance.

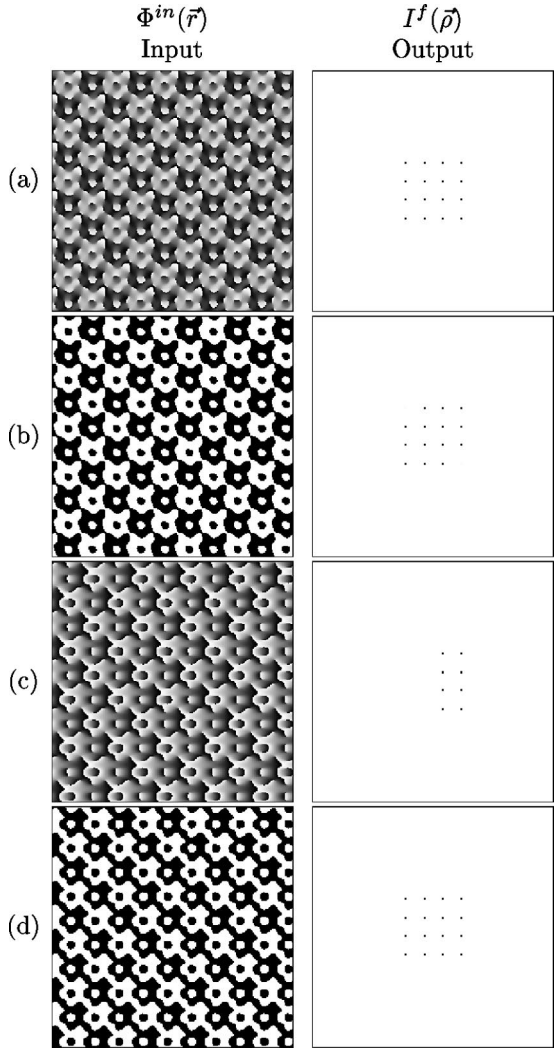

FIG. 4. Inversion symmetry in binarized holograms. (a) A continuous hologram encoding a 4×4 array of tweezers. (b) The binary version generates an array with missing tweezers. (c) A continuous hologram encoding a 4×2 array of tweezers. (d) The binary version of hologram (c) makes a satisfactory 4×4 array of tweezers.

B. Tiling

Because FFTs yield periodic functions, all holograms calculated with the AA algorithm can be tiled smoothly. That is, they can serve as the unit cell for new holograms without introducing phase discontinuities at the unit cell boundaries. The result of such tiling is to increase the spacing between tweezers by an amount proportional to the number of tilings along each dimension without reducing the resolution or trapping ability of the individual tweezers. Figure 5 shows successive tilings of a hologram that generates a 3×3 square array of tweezers, each labeled by the number of unit cells tiled along each side of the hologram. The same number describes the relative spacings of the resulting tweezers.

We use this property to design holograms encoding tweezer arrays with large inter-tweezer spacings. Increasing an array's lattice constant requires smaller features in the input plane. In order to resolve these small features, the hologram's pixel size must be reduced. Since the width of the hologram is fixed, the number of pixels increases with the inverse square of the pixel size. Calculating such holograms can become computationally expensive. Instead of directly calculating the hologram for a desired lattice constant, therefore, we calculate the smaller hologram encoding the same pattern with a proportionately smaller lattice constant. This hologram can be tiled to create a hologram for the desired tweezer spacing. Tiling can be done either numerically or physically, via a step and repeat mask fabrication process.

VI. FABRICATION

Phase profiles can be recorded in the surface topography of an optical element,[14] or in controlled variations in a dielectric's index of refraction.[5] Liquid crystal displays also have been used as phase-modulating elements,[15] and dynamically reconfigurable patterns of beams suitable for forming optical tweezer arrays have been demonstrated,[16] although not yet used to make three-dimensional traps. Some photorefractive elements such as those being explored as optical memory devices also can be reconfigured, but must be programmed optically. Few, if any, are available as commercial optical elements. Photorefractive holograms created with photographic techniques[5] promise the greatest flexibility for creating static tweezer arrays at very low cost, but do not appear to have advanced beyond the research stage.

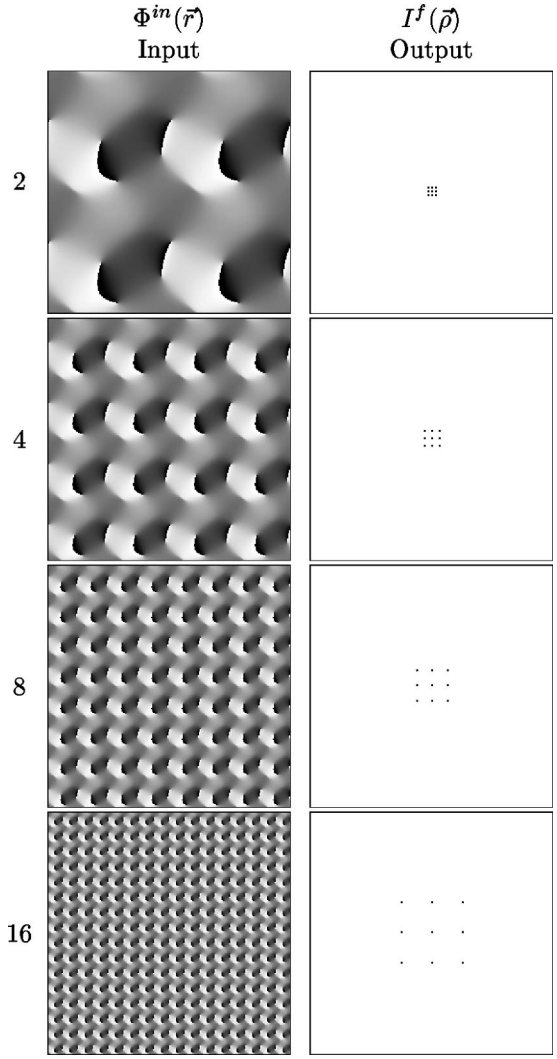

FIG. 5. Tiling a hologram encoding a 3×3 array of tweezers scales the spacing between tweezers without sacrificing resolution. Marginal numbers indicate the number of copies tiled into each side.

Surface patterning takes advantage of well-established photolithographic techniques and can be implemented easily and inexpensively. We have taken this approach in creating our own holographic optical tweezer arrays. Figure 6 shows the principle. Light propagates more slowly in a dielectric material than in air. When a wave front first enters the material, it is uniformly slowed to a speed c/n, where c is the speed of light in vacuum and n is the material's index of refraction. Parts of the wave front emerging first from the textured surface propagate at speed c, while sections remaining in the material fall behind, picking up a phase delay proportional to the extra thickness of material. Consequently, the relative phase at $\mathbf{r}$ is proportional to the surface's relief, $d(\mathbf{r})$:

$$\Phi^{\text{in}}(\mathbf{r}) = 2\pi(n-1)\frac{d(\mathbf{r})}{\lambda}. \tag{18}$$

A similar principle applies when imposing a pattern of phase delays through the relief on a reflective surface, but with the factor $n-1$ replaced by 2.

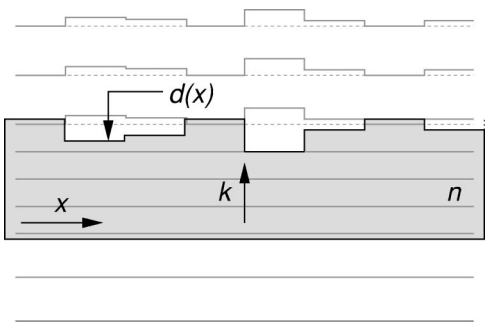

FIG. 6. Encoding phase in surface profile. A plane wave incident upon the flat side of a transparent dielectric material acquires a spatially modulated phase upon passing through its textured surface.

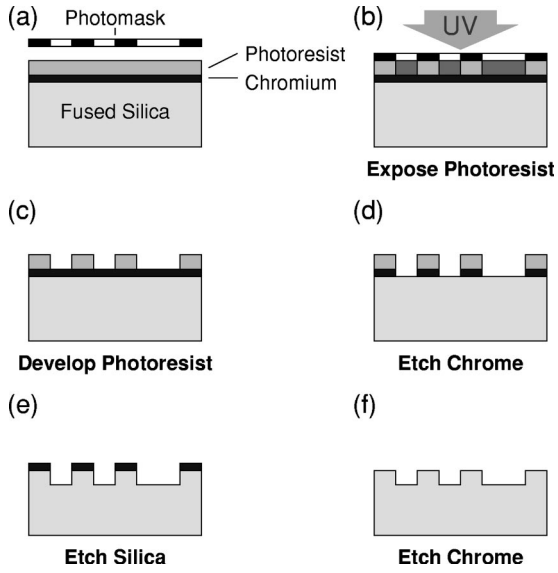

FIG. 7. Fabricating holograms with reactive ion etching.

The pattern of hills and valleys needed to create a desired phase profile can be formed in photoelastic polymer gels. Such materials provide the recording medium for commercial holographic printers. These are not so common as photolithographic facilities for surface etching, however, so we digress in the next section to describe the details of our fabrication process.

A. Reactive ion etching of fused silica

We employ reactive ion etching to create binary holograms in 1-mm-thick substrates of polished fused silica, a transparent medium with an index of refraction of $n = 1.456$ at the wavelength of our trapping laser, $\lambda = 532$ nm. Obtaining a phase shift of π radians requires a feature depth of $\lambda/(2n-2) = 583$ nm. The fabrication process has three main steps: creating a photomask, transferring this pattern to an etch mask covering the silica, and then etching to a precise depth, Fig. 7.

High contrast, high resolution film can be used to create masks for many of the trapping patterns we have investigated. We begin by laser printing the calculated phase profile as a binary image, with black pixels representing a relative phase shift of π radians, and white representing 0 radians. This image is photoreduced to the actual dimensions of the hologram. Each of our holograms covers a square whose

width, $2f=3.24$ mm, matches the laser beam's diameter at B^* in Fig. 1. Holograms involving finer linewidths were vectorized before processing with commercial mask writers at the National Nanofabrication Facility.

We next create an etch mask on the surface of the fused-silica substrate. First the surface is protected with a 25 nm layer of chromium and a 1.76 μm layer of positive photoresist, Fig. 7(a). The photomask is placed in contact with the photoresist, and the entire sample is exposed to UV radiation, Fig. 7(b). The photomask is removed and exposed regions of the photoresist are dissolved away, revealing parts of the chromium layer, Fig. 7(c). Finally, the exposed chromium is removed with an acid wash, exposing the sections of silica to be etched, Fig. 7(d).

Unprotected regions of the silica are susceptible to attack by fluoride ions. Reactive ion etching provides a controlled exposure to ions generated by rf dissociation of a mixture of oxygen and carbon tetrafluoride. These reactive ions rapidly oxidize the organic photoresist, but are halted by the layer of metallic chromium. The unprotected regions of the silica surface continue to be removed at a rate of about 0.5 nm/s, Fig. 7(e), until the etched regions reach the desired depth. As the final step, we remove the remaining chromium to reveal a precisely textured fused-silica surface, Fig. 7(f).

The etching process could be repeated with different photomasks to produce a more nuanced pattern.[14] N such steps would yield 2^N gradations of phase delay. Each step, however, would require planarizing and polishing the previously etched pattern, recoating the surface, and precisely aligning the new photomask over the existing pattern before etching. Not only is this time consuming, it is not necessary for many applications.

B. Tolerances

Regardless of the fabrication method, any practical phase hologram will deviate from its design and these deviations will degrade its performance. We consider two principal fabrication defects: overall multiplicative error in the phase modulation due to mismatches between wavelength and etch depth, and random noise in the local phase shift due to roughness. To quantify these defects' influence on hologram performance, we define the efficiency, $\mathcal{E}$, to be the fraction of incident laser power projected into the planned tweezer pattern. For simplicity, we compare the intensity pattern in the focal plane when the actual hologram is illuminated by a uniform plane wave, $\tilde{I}^f(\boldsymbol{\rho})$, to the ideal intensity pattern in the focal plane, $I_0^f(\boldsymbol{\rho})=(2\pi f/k)^2T^2(\boldsymbol{\rho})$. The corresponding efficiency

$$\mathcal{E}\equiv\frac{\sum_{i=1}^{M^2}T^2(\boldsymbol{\rho}_i)\tilde{I}^f(\boldsymbol{\rho}_i)}{\sum_{i=1}^{M^2}T^2(\boldsymbol{\rho}_i)} \tag{19}$$

is a less stringent measure of the agreement between the ideal and actual holograms than the error, ϵ_n, since it is possible to have $\mathcal{E}=1$ when $\epsilon_n>0$, but $\epsilon_n=0$ implies $\mathcal{E}=1$.

To give a feel for the results obtained with our methods, we calculate the efficiency of four standard holograms as a function of the severity of the fabrication defects. The four standard holograms are continuous and binary versions of patterns encoding 4×4 and 20×20 square tweezer arrays, each with the same lattice constant. We calculated all four holograms 20 times, and selected the most efficient hologram from each group to use in the efficiency studies.

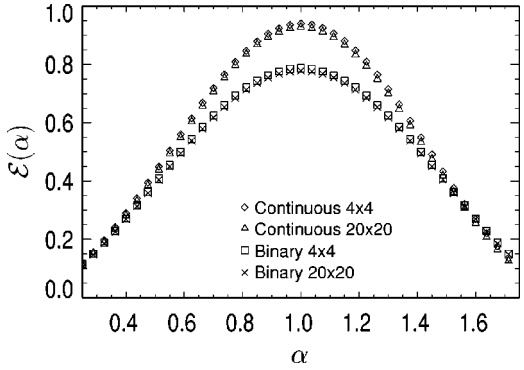

FIG. 8. Influence of phase errors on projection efficiency. Symbols indicate numerically calculated efficiencies for continuous and binary holograms encoding 4×4 and 20×20 square arrays of tweezers.

The phase modulation created by an etched hologram is proportional to the etch depth, Eq. (18). If the etch rate is not precisely controlled, or if the hologram is illuminated with light of the wrong wavelength, the actual phase profile, $\tilde{\Phi}^{\text{in}}(\mathbf{r})$, will differ from the design $\Phi^{\text{in}}(\mathbf{r})$ by a scale factor, $\tilde{\Phi}^{\text{in}}(\mathbf{r})=\alpha\Phi^{\text{in}}(\mathbf{r})$. As α departs from unity, most of the laser light not contributing to the tweezer array is focused at the central undiffracted spot. Figure 8 shows the efficiency, $\mathcal{E}(\alpha)$, of the four standard holograms as a function of α. Even the continuous holograms with $\alpha=1$ are not perfectly efficient because the AA algorithm rarely identifies a globally ideal phase modulation. Binary holograms are still less efficient, with ideal efficiencies near 80%. Reassuringly, Fig. 8 suggests that a hologram's efficiency does not depend strongly on precisely matching etch depth to the light's wavelength.

Even if the overall etch depth is carefully controlled, reactive ion etching creates a rough surface, whose asperities add random fluctuations to the phase profile. We measured the surface topography of our fused-silica wafers after etching and found a Gaussian distribution of etch depths, with a standard deviation of 60 nm or $\pi/10$ radians at 532 nm illumination. This roughness is laterally uncorrelated down to length scales of less than 280 nm.

We gauged roughness influence on the holograms' efficiencies by adding uncorrelated Gaussian noise to the *calculated* optimal phase profiles

$$\tilde{\Phi}^{\text{in}}(\mathbf{r})=\Phi^{\text{in}}(\mathbf{r})+\eta(\mathbf{r}), \tag{20}$$

where the noise's probability distribution is given by

$$\rho(\eta)=\frac{1}{\sqrt{2\pi\sigma_\Phi^2}}\exp\left(-\frac{\eta^2}{2\sigma_\Phi^2}\right). \tag{21}$$

Figure 9 shows how the efficiency, $\mathcal{E}(\sigma_\Phi)$, of the four standard holograms decreases with increasing surface roughness, σ_Φ.

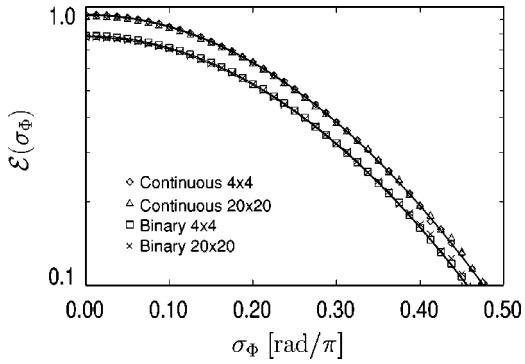

FIG. 9. Influence of roughness on efficiency. Symbols indicate numerically calculated efficiencies for continuous and binary holograms encoding 4×4 and 20×20 square arrays of tweezers subject to random Gaussian phase noise of magnitude σ_Φ. Solid curves show the corresponding ensemble-averaged predictions from Eq. (24).

Combining Eqs. (4) and (20) yields the electric field profile in the focal plane for a given manifestation of the noise profile in the input plane

$$\tilde{E}^f(\boldsymbol{\rho}) = \frac{k}{2\pi f}\int d^2r\, \exp\left(i\frac{k}{f}\mathbf{r}\cdot\boldsymbol{\rho} + i\Phi^{\text{in}}(\mathbf{r}) + i\,\eta(\mathbf{r})\right). \tag{22}$$

Averaging over all possible phase profiles yields

$$\langle \tilde{E}^f(\boldsymbol{\rho})\rangle = \exp(-\tfrac{1}{2}\sigma_\Phi^2)E^f(\boldsymbol{\rho}) \tag{23}$$

so that

$$\langle \mathcal{E}(\sigma_\Phi)\rangle = \mathcal{E}(0)\exp(-\sigma_\Phi^2). \tag{24}$$

This result agrees well with numerically calculated efficiencies, as can be seen in Fig. 9. Substituting the measured σ_Φ^2 for our etched binary holograms, we estimate that roughness diminishes their efficiencies by a further 10% to roughly 70%.

VII. FURTHER CONSIDERATIONS

Using the techniques described above, we have created triangular and square tweezer arrays which trap up to 400 particles at once. Still larger arrays and less regular arrangements are certainly feasible. Even static holograms permit some degree of reconfigurability. Rotating a hologram about its optical axis rotates the pattern of tweezers in the plane. Tilting it changes the aspect ratio. Individual traps can be turned off by blocking their beams in the plane conjugate to the object plane, labeled OP* in Fig. 1. Such spatial filtering also can be useful for eliminating stray laser light, and to block out any undiffracted portion of the input beam. Replacing lenses L1 and L2 with zoom lenses should permit a degree of continuous scaling of the lattice constant.

The methods described in the previous sections are appropriate for projecting arrays of identical tweezers in the plane, where each tweezer shares the properties of a single tweezer formed by the unmodulated input beam. Shaping the wave fronts of the individual beams, for example, to embed some optical vortices in an array of conventional optical tweezers, requires a straightforward elaboration of the AA algorithm.[13] Creating three-dimensional arrays, on the other hand, requires more sophisticated calculations to avoid undesirable interference effects, and will be discussed elsewhere.

ACKNOWLEDGMENTS

This work was funded by the National Science Foundation through Grant No. DMR-9730189, by the MRSEC program of the NSF through Grant No. DMR-9888595 and by the David and Lucile Packard Foundation. G. C. S. was supported by an award from the Research Corporation.

[1] A. Ashkin, J. M. Dziedzic, J. E. Bjorkholm, and S. Chu, Opt. Lett. **11**, 288 (1986).
[2] K. Svoboda and S. M. Block, Annu. Rev. Biophys. Biomol. Struct. **23**, 247 (1994); A. Ashkin, Proc. Natl. Acad. Sci. U.S.A. **94**, 4853 (1997); A. Ashkin, J. M. Dziedzic, and T. Yamane, Nature (London) **330**, 769 (1987); S. B. Smith, L. Finzi, and C. Bustamante, Science **258**, 1122 (1992); C. Bustamante *et al.*, *ibid.* **265**, 1599 (1994); T. T. Perkins *et al.*, *ibid.* **268**, 83 (1995); H. Yin *et al.*, *ibid.* **270**, 1653 (1995); K. König *et al.*, Cell. Mol. Bio. **42**, 501 (1996); M. D. Wang *et al.*, Biophys. J. **72**, 1335 (1997).
[3] D. G. Grier, Curr. Top. Colloid Interface Sci. **2**, 264 (1997); R. Bar-Ziv, Phys. Rev. Lett. **73**, 1392 (1994); J. C. Crocker and D. G. Grier, **73**, 352 (1994); R. Bar-Ziv *et al.*, *ibid.* **75**, 3356 (1995); J. C. Crocker and D. G. Grier, Phys. Rev. Lett. **77**, 1897 (1996); A. D. Dinsmore, A. G. Yodh, and D. J. Pine, Nature (London) **383**, 239 (1996); T. Sugimoto *et al.*, Langmuir **13**, 5528 (1997); J. Crocker, J. Chem. Phys. **106**, 2837 (1997); J. C. Crocker, J. A. Matteo, A. D. Dinsmore, and A. G. Yodh, Phys. Rev. Lett. **82**, 4352 (1999); J.-C. Meiners and S. R. Quake, *ibid.* **82**, 2211 (1999).
[4] E. R. Dufresne and D. G. Grier, Rev. Sci. Instrum. **69**, 1974 (1998); D. G. Grier and E. R. Dufresne, U.S. Patent No. 6,055,106 (2000).
[5] H. He, N. R. Heckenberg, and H. Rubinsztein-Dunlop, J. Mod. Opt. **42**, 217 (1995).
[6] K. T. Gahagan and J. G. A. Swartzlander, Opt. Lett. **21**, 827 (1996); N. B. Simpson, L. Allen, and M. J. Padgett, J. Mod. Opt. **43**, 2485 (1996).
[7] P. C. Ke and M. Gu, J. Mod. Opt. **45**, 2159 (1998).
[8] S. Nemoto and H. Togo, Appl. Opt. **37**, 6386 (1998).
[9] P. A. Maia Neto and H. M. Nussenzveig, Europhys. Lett. **50**, 702 (2000).
[10] E. Fällman and O. Axner, Appl. Opt. **36**, 2107 (1997).
[11] C. Mio, T. Gong, A. Terray, and D. W. M. Marr, Rev. Sci. Instrum. **71**, 2196 (2000).
[12] S. G. Lipson and H. Lipson, *Optical Physics*, 2nd ed. (Cambridge University Press, Cambridge, 1981).
[13] V. Soifer, V. Kotlyar, and L. Doskolovich, *Iterative Methods for Diffractive Optical Elements Computation* (Taylor & Francis, Bristol, PA, 1997).
[14] G. J. Swanson and W. B. Veldkamp, Opt. Eng. (Bellingham) **28**, 605 (1989).
[15] Y. Igasaii *et al.*, Opt. Rev. **6**, 339 (1999).
[16] M. Reicherter, T. Haist, E. U. Wagemann, and H. J. Tiziani, Opt. Lett. **24**, 608 (1999); P. C. Mogensen and J. Gluckstad, Opt. Commun. **175**, 75 (2000).